Isolated hydrogen configurations in zirconia as seen by muon spin spectroscopy and *ab initio* calculations

R. B. L. Vieira,[1,*] R. C. Vilão,[1] A. G. Marinopoulos,[1] P. M. Gordo,[1] J. A. Paixão,[1] H. V. Alberto,[1] J. M. Gil,[1] A. Weidinger,[2] R. L. Lichti,[3] B. Baker,[3] P. W. Mengyan,[4] and J. S. Lord[5]

[1]*CFisUC, Department of Physics, University of Coimbra, P-3004-516 Coimbra, Portugal*

[2]*Helmholtz-Zentrum Berlin für Materialien und Energie, 14109 Berlin, Germany*

[3]*Department of Physics, Texas Tech University, Lubbock, Texas 79409-1051, USA*

[4]*Department of Physics, Northern Michigan University, Marquette, Michigan 49855, USA*

[5]*ISIS Facility, Rutherford Appleton Laboratory, Chilton, Didcot, Oxon OX11 0QX, United Kingdom*

(Received 9 June 2016; revised manuscript received 25 August 2016; published 26 September 2016)

We present a systematic study of isolated hydrogen in diverse forms of ZrO_2 (zirconia), both undoped and stabilized in the cubic phase by additions of transition-metal oxides (Y_2O_3, Sc_2O_3, MgO, CaO). Hydrogen is modeled by using muonium as a pseudoisotope in muon-spin spectroscopy experiments. The muon study is also supplemented with first-principles calculations of the hydrogen states in scandia-stabilized zirconia by conventional density-functional theory (DFT) as well as a hybrid-functional approach which admixes a portion of exact exchange to the semilocal DFT exchange. The experimentally observable metastable states accessible by means of the muon implantation allowed us to probe two distinct hydrogen configurations predicted theoretically: an oxygen-bound configuration and a quasiatomic interstitial one with a large isotropic hyperfine constant. The neutral-oxygen-bound configuration is characterized by an electron spreading over the neighboring zirconium cations, forming a polaronic state with a vanishingly small hyperfine interaction at the muon. The atom-like interstitial muonium is observed also in all samples but with different fractions. The hyperfine interaction is isotropic in calcia-doped zirconia [$A_{iso} = 3.02(8)$ GHz], but slightly anisotropic in the nanograin yttria-doped zirconia [$A_{iso} = 2.1(1)$ GHz, $D = 0.13(2)$ GHz] probably due to muons stopping close to the interface regions between the nanograins in the latter case.

DOI: 10.1103/PhysRevB.94.115207

I. INTRODUCTION

Zirconia is a ceramic material with diverse uses such as an oxygen sensor [1], thermal-barrier coating [2], and cladding material for nuclear reactors [3], and it is under consideration as a possible high-permittivity (κ) gate dielectric in metal-oxide-semiconductor devices [4]. Zirconia is also commonly used as the solid electrolyte in solid-oxide fuel cell technology [5]. The relevant phase of zirconia in this case is the cubic phase (Fig. 1) rather than the ground-state monoclinic phase owing to superior mechanical and electrical properties of the former. In fact, pure zirconia presents a monoclinic structure at low temperatures which changes into tetragonal at about 1400 K and into cubic at about 2650 K. At low temperatures the cubic phase is stabilized by suitable doping with trivalent or divalent metal oxides (Y_2O_3, Sc_2O_3, MgO, CaO) which also leads to the formation of oxygen vacancies in the lattice as charge-compensating defects.

Hydrogen is a ubiquitous impurity in materials and zirconia is not an exception. Its effects for this oxide (notably its cubic-stabilized phase) have been principally related to proton conduction at low and intermediate temperatures [6,7]. Hydrogen is frequently incorporated during processing and it can dominate the properties of many oxides. The investigation of the role of hydrogen in semiconductors and oxides has assumed increasing and vital importance since the discovery that this impurity can be the source of *n*-type conductivity in II-VI semiconducting compounds [8,9]. This subject has seen notable advances from the interplay of theoretical predictions from calculations based on density-functional theory (DFT) and muon-spin rotation (μSR) spectroscopy [10–14].

From the experimental point of view, the use of muonium (the hydrogenic atom possessing a positive muon as the nucleus: μ^+e^-) as a light pseudoisotope of hydrogen has become standard in order to obtain information regarding the electronic states of isolated hydrogen in materials [15–18]. Although the muon is only one-ninth the mass of the proton, the reduced mass of muonium is 99.6% that of hydrogen, so that the respective electronic properties are basically the same in both atoms. Muonium spectroscopy has the particular advantage of corresponding to the high-dilution limit for the muonium impurity, which can thus quite generally be considered isolated and is affected only indirectly by other defects and impurities (including hydrogen impurities) through the overall Fermi energy. Extensive studies have thus been carried out to characterize the muonium centers formed in different semiconductors and oxides [12,13,19–21] and the respective results for the muonium configurations compare well with those obtained with protons, for the very few cases allowing comparison [9,22–25].

From a theory standpoint, hydrogen states in zirconia have been studied in the past by first-principles calculations; nonetheless with the exception of an earlier attempt by μSR [19] a detailed experimental confirmation and analysis is still largely lacking. More specifically, DFT-based calculations determined the type of hydrogen configurations and defect electrical levels for hydrogen in the monoclinic [26,27], the ideal cubic [28,29] and tetragonal [30], and the cubic yttria-stabilized [31] phases. For bulk crystalline YSZ [31],

*vieira.fis@gmail.com

 ©2016 American Physical Society

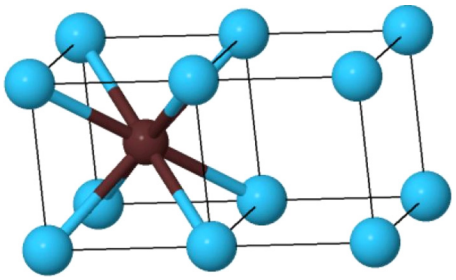

FIG. 1. Schematic of a portion of the undistorted fluorite cubic lattice of zirconia, showing the alternance between cubes with and without a Zr cation. Blue spheres represent oxygen anions and the dark brown sphere represents the zirconium cation.

in particular, the calculations showed that hydrogen is an amphoteric impurity and a negative-U defect with the pinning level, $E(-/+)$, lying deep inside the gap. Hydrogen behaved similarly in the pure monoclinic phase both in zirconia [27] and in the isovalent and isostructural hafnia [27,32], with both studies employing hybrid-functional approaches.

In the present study we employ μSR spectroscopy aided by first-principles calculations to determine the type of hydrogen configurations in a number of zirconia phases, both undoped and stabilized in the cubic phase by additions of metal oxides (Y_2O_3, Sc_2O_3, MgO, CaO). The theoretical and experimental details are presented in Sec. II. In Sec. III we present the results concerning the identification of an oxygen-bound configuration with small hyperfine interaction and of an atomic-like interstitial configuration with large hyperfine interaction, as well as the temperature-activated transition from interstitial to oxygen bound. Our conclusions are summarized in Sec. IV.

II. METHODOLOGICAL DETAILS

A. Experimental details

Muon-spin rotation and relaxation experiments took place at the EMU instrument of the ISIS Facility, Rutherford Appleton Laboratory, United Kingdom. In the experiments the following polycrystalline samples were used: an undoped monoclinic ZrO_2 sample (obtained commercially from Alfa Aesar), a scandia-stabilized ZrO_2 sample (ScSZ, obtained commercially from Sigma-Aldrich), an yttria-stabilized ZrO_2 sample (YSZ, kindly provided by INNOVNANO), a magnesia-partially-stabilized ZrO_2 sample (MgSZ, obtained commercially from Goodfellow), and two calcia-doped ZrO_2 samples (ZrO_2:Ca and CaSZ, obtained commercially from Alfa Aesar).

The crystallographic structure of the samples was verified using x-ray diffraction (XRD). XRD patterns were collected over a 2θ range of 10°–135° in steps of 0.01° and an exposition of 2 s per step using a Bruker D8 Advance diffractometer with Cu Kα radiation. The data were analyzed by the Rietveld method using the TOPAS software [33]. The results are summarized in Table I. We note that the local structures of the cubic and of the tetragonal phases are very similar and distinct from the monoclinic local structure [34].

Conventional transverse-field and longitudinal-field μSR measurements were undertaken from liquid-helium temperature up to 700 K. The samples were stored and handled in air. During the measurements, the samples were in low-pressure helium exchange gas. No significant structural change with ambient atmosphere is expected to occur for temperatures below 1000 K. The typical hydrogen content in crystalline zirconia is on the order of 1×10^{18} cm^{-3} [35]. This concentration is high with respect to usual doping levels but it is small enough that no direct interaction with randomly stopped single muons is expected. There is also no long-range electrical activity in these insulating samples. The present data thus concern isolated muonium, as a model for isolated hydrogen, in an intrinsic surrounding, and the interaction with hydrogen atoms in the sample can be neglected.

In Fig. 2 we present a typical transverse-field time spectrum obtained for ScSZ, at $T = 7.8$ K and with an applied transverse field $B = 10$ mT. We note that, despite the overall differences between the samples (doping, crystallographic structure, grain size, as expressed in Table I), all samples show a remarkably similar behavior, which expresses the local nature of the muon probe. A clear slightly damped oscillation at the Larmor frequency $\omega/2\pi = (\gamma_\mu/2\pi)B = 1.39$ MHz is observed, corresponding to muons forming a diamagnetic component. However a fit using a single relaxing oscillation does not model correctly the low-temperature time spectra. An additional component with a higher relaxation, corresponding to muons forming a paramagnetic component, is needed. We have thus fitted the data with a sum of two components:

$$A(t) = A_d e^{-\frac{1}{2}\sigma^2 t} \cos(\omega t + \phi_d) + A_{p_1} e^{-\lambda_{p_1} t} \cos(\omega t + \phi_{p_1}), \quad (1)$$

where A_d and A_{p_1} are respectively the diamagnetic and paramagnetic asymmetries, σ is the Gaussian diamagnetic relaxation, λ_{p_1} is the Lorentzian paramagnetic relaxation, and

TABLE I. List of samples used in this work together with crystallographic details verified with x-ray diffraction. Errors in phase abundance are indicated only when at least two phases were clearly identified.

		Crystal structure			Grain size		
Sample designation	Composition	Cubic %	Tetragonal %	Monoclinic %	Cubic (nm)	Tetragonal (nm)	Monoclinic (nm)
ZrO_2 (undoped)	ZrO_2			100			79.4(5)
ScSZ	$(Sc_{0.1}Zr_{0.9})O_{1.95}$	35(1)	65(1)		76(6)	17.9(5)	
YSZ	$(Y_{0.08}Zr_{0.92})O_{1.96}$	100			12.7(1)		
MgSZ	$(Mg_{0.04}Zr_{0.96})O_{1.96}$	30.6(4)	41.6(4)	27.8(3)	27.0(5)	34.3(6)	30.8(8)
ZrO_2:Ca (monoclinic)	$(Ca_{0.06}Zr_{0.94})O_{1.94}$			100			48.8(7)
CaSZ	$(Ca_{0.06}Zr_{0.94})O_{1.94}$	81(1)		19(1)	70(3)		20(2)

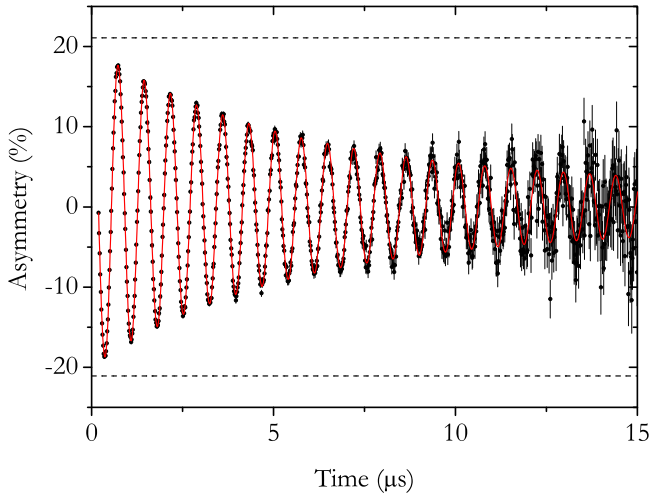

FIG. 2. Muon spin asymmetry as a function of time, in transverse geometry ($B = 10$ mT), at $T = 7.8$ K, for the ScSZ sample. The maximum instrumental asymmetry is indicated (horizontal dashed lines), showing the existence of an unobserved fraction of muon spin polarization (missing fraction). A rapidly decaying component is prominent in the first 6 μs, superimposed on a slowly relaxing component dominant for higher times.

ϕ_d and ϕ_{p_1} are respectively the diamagnetic and paramagnetic phases.

For the MgSZ and the calcia-doped samples (CaSZ and monoclinic ZrO_2:Ca), an additional paramagnetic relaxing component with a relaxation of about 10 times higher is present. These data were thus fitted with a sum of three components:

$$A(t) = A_d e^{-\frac{1}{2}\sigma^2 t}\cos(\omega t + \phi_d) + A_{p_1} e^{-\lambda_{p_1} t}\cos(\omega t + \phi_{p_1}) + A_{p_2} e^{-\lambda_{p_2} t}\cos(\omega t + \phi_{p_2}), \quad (2)$$

where the subscripts p_1 and p_2 denote the slower and faster relaxing paramagnetic component, respectively.

Data analysis were completed with the WiMDA program [36]. A room temperature calibration with a silver sample at $B = 10$ mT allowed us to extract the maximum instrumental asymmetry $A_{\max}$ and therefore to measure the fraction of muons thermalizing at each configuration.

B. Theoretical framework

For the first-principles study of the hydrogen states in ScSZ we employed two different approaches. First, density-functional theory (DFT) [37,38] within the generalized-gradient approximation (GGA) for exchange and correlation. The standard semilocal PBE [39] functional introduced by Perdew, Burke, and Ernzerhof was used in this case. The second approach was the hybrid HSE06 functional [40,41] where a portion of exact Fock exchange is admixed to the semilocal PBE exchange. Hybrid functionals reduce the self-interaction error which is inherent in local and semilocal DFT functionals; HSE06, in particular, has been shown to provide band gaps in solids in very good agreement with experiment [42]. In either case the calculations were based on the projector-augmented wave (PAW) method [43,44] using pseudopotentials to account for the valence-core interaction. The most recent implementations currently distributed in the VASP code [45–47] were employed. The crystalline wave functions were expanded in a plane-wave basis that was limited by a kinetic-energy cutoff of 420 eV. Although this cutoff provided converged structural properties and formation energies, additional tests with higher cutoffs (of up to 550 eV) were performed to examine the convergence behavior of the hyperfine parameters for neutral hydrogen. These parameters were determined within the PAW methodology [48,49] which allows the reconstruction of the all-electron wave functions inside the core regions of the nuclei.

The defect calculations were carried out on 96-atom supercells of cubic zirconia with a 10.3% mol scandia (Sc_2O_3) concentration. The cells were constructed by initially building a $2 \times 2 \times 2$ supercell by doubling the dimensions of the simple cubic (fluorite) cell of ZrO_2. For the latter we have assumed a lattice parameter equal to 5.09 Å which is the experimental lattice parameter of cubic ScSZ at the prescribed scandia concentration [50,51]. The desired scandia doping was then achieved by introducing the necessary formula units of Sc_2O_3 to these zirconia supercells. More specifically, six Sc atoms were inserted substitutionally in the cation sublattice at random positions and three charge-compensating oxygen vacancies were also created in the anion sublattice.

The formation energies $E_{\text{form}}(H^q)$ of hydrogen were determined for each of its charge states, q, as a function of the Fermi-level position E_F in the gap. The expression for $E_{\text{form}}(H^q)$ is

$$E_{\text{form}}(H^q) = E_{\text{tot}}(H^q) - E_{\text{tot}}(\text{bulk}) - \mu_{\text{H}} + q(E_F + E_{\text{V}}), \quad (3)$$

where $E_{\text{tot}}(H^q)$ is the total energy of the supercell with hydrogen in the charge state q ($q = -1, 0$, or $+1$) and $E_{\text{tot}}(\text{bulk})$ the total energy of the bulk-crystal ScSZ supercell. μ_{H} is the chemical potential of hydrogen and was taken here as half the energy of a hydrogen molecule at $T = 0$ K. E_{V} is the energy of the valence-band (VB) edge of the bulk ScSZ supercell and provides the reference energy for the values of E_F in the gap.

III. RESULTS AND DISCUSSION

A. Theory

In an initial stage the semilocal DFT functional was used to obtain the minimum-energy supercells of the bulk crystalline ScSZ cubic phase. A total of ten trial ScSZ supercells were constructed with various associations between the Sc ions and the oxygen vacancies. The ensuing energy minimization led to final minimum-energy configurations which entailed important structural distortions with respect to the starting (ideal) fluorite cells. The anion sublattice exhibited the larger distortions with some of the oxygen ions displacing as far as 0.8 Å away from their ideal fluorite sites, in accordance with previous theoretical studies of cubic stabilized zirconia with similar content of stabilizing oxides [31,52]. The lowest-energy supercell was structurally similar to the one determined for yttria-stabilized zirconia in our previous work [31] and was subsequently used for the defect calculations. The resulting

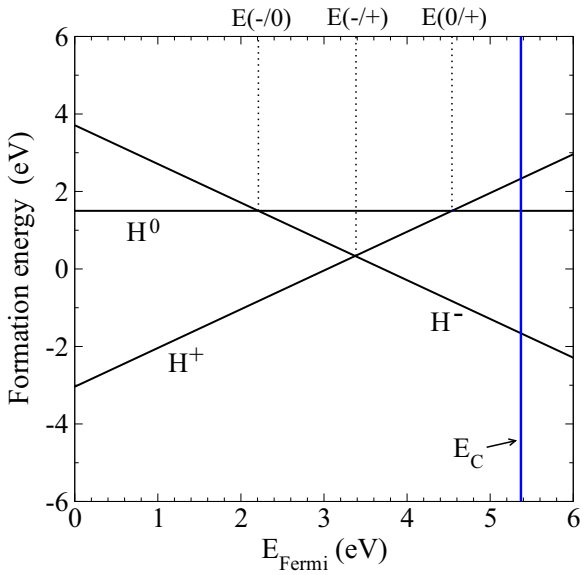

FIG. 3. Formation-energy plot of the different charge states of hydrogen as a function of the Fermi-level position in the gap. The plot shows the results obtained by the hybrid-functional (HSE06) approach. The thermodynamic charge-transition levels, $E(q/q')$, are denoted by the vertical lines. The valence-band (VB) edge defines the reference energy for the Fermi level which spans the band gap up to the conduction-band minimum (E_C). The plot depicts the formation energies of the lowest-energy structures that hydrogen forms in the ScSZ cell for each of its charge states.

formation energies, transition levels, and hyperfine parameters were determined for both functionals. In the present study a percentage of 25% was chosen for exact exchange when employing the HSE06 functional. This led to an energy gap equal to 5.37 eV, a value consistent with existing experimental reports of stabilized cubic zirconia and results of other first-principles calculations of yttria-stabilized zirconia of similar yttria content [31,52].

Hydrogen was subsequently introduced in various positions in the lowest-energy ScSZ supercell and the resulting minimum-energy structures were determined by both functionals. Hydrogen was found to adopt hydroxide-bond configurations, namely forming an OH^- bond with the oxygen ions of the ScSZ lattice. Typically OH^- bond lengths were in the 0.98–1.00 Å range with hydrogen distances to a next-nearest anion spanning a larger range (from 1.60 to 2.20 Å). Whereas protons (H^+) were exclusively encountered in such configurations, both H^0 and H^- were further found to reside in the empty interstitial sites of the fluorite lattice (see Fig. 1). H^- in particular preferably occupies these interstitial sites with much lower formation energies. H^- was further found to be stabilized at the oxygen-vacancy sites, namely as a substitutional defect in the anion sublattice.

The formation-energy plot for the low-energy charge states of hydrogen is shown in Fig. 3, as a function of the Fermi-level position in the band gap, E_{gap}. In the same figure the thermodynamic charge-transition levels are indicated by the vertical lines. These results show that a single hydrogen impurity is an amphoteric defect in cubic ScSZ with the pinning level $E(-/+)$ lying well within the energy gap of

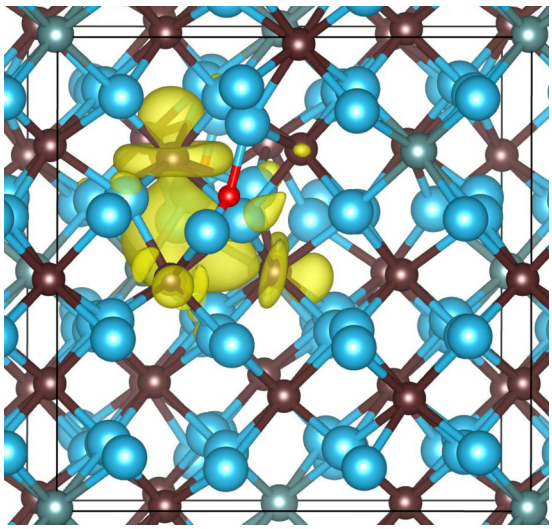

FIG. 4. Atomistic structure of a neutral oxygen-bound hydrogen configuration in ScSZ obtained from the hybrid (HSE06) calculations. The spin-density isosurface reveals the localization of the excess electron (shown in yellow). The chemical elements are represented as H (very small red sphere), Zr (small dark brown spheres), O (large blue spheres), Sc (medium-sized light-gray spheres).

the host. This is consistent with the behavior of hydrogen in cubic YSZ [31] and in the monoclinic phase of pure zirconia [27] and pure hafnia [27,32]. Furthermore, in our calculations both the acceptor and donor levels, $E(-/0)$ and $E(0/+)$, respectively, are deep levels that lie appreciably away from the respective bands edges (E_V and E_C), with positions at $E(-/0) = E_V + 2.21$ eV and $E(0/+) = E_C - 0.83$ eV. These results suggest that thermal ionization of neutral hydrogen at low and moderate temperatures is extremely difficult. The calculated formation energies further show that neutral H is never the lowest-energy charge state of H under conditions of thermodynamic equilibrium. Nonetheless, H^0 is a well-defined stable state (albeit of high energy) whose existence and properties can be probed by μSR at sufficiently short time scales where thermodynamic equilibrium may not be attainable. The reported μSR spectra and analysis in the present study have indeed shown this. It was therefore deemed necessary to perform a more exhaustive study of the properties of the H^0 paramagnetic defect and, in particular, examine its electron density and hyperfine signature by theoretical means.

The localization properties of the electron of neutral hydrogen, H^0, was characterized in detail for a number of oxygen-bound H^0 configurations. For the one with the lowest-formation energy the corresponding spin-density profile calculated by HSE06 (shown in Fig. 4) suggests clearly that neutral hydrogen in ScSZ is not a shallow-donor defect. Instead, the electron possesses a very compact (localized) 4*d*-type rather than a delocalized character, confirming its deep-donor nature as inferred from the formation-energy plot (see Fig. 3). It can also be seen that the spin localization is neither spherical nor axially symmetric. The electron is trapped at neighboring Zr ions, with an asymmetric distribution: the spin density displays a more dominant weight on a Zr ion located at a distance of 3.9 Å to the hydrogen nucleus, towards the upper-left corner of the supercell (see Fig. 4).

The isosurface profile also shows considerable weight of the excess electron in the interstitial space of the fluorite lattice. Inspection of the displacement field near the defect further showed that the excess electron polarizes locally the oxide lattice: in particular, the Zr-O distances around the Zr ion which carries the largest electron density increase by as much as 0.10 Å in order to accommodate the extra electron. This is a signature of a small-polaron formation induced by the presence of the hydrogen electron, which in turn becomes trapped near the impurity site. This outcome was confirmed by examining several other oxygen-bound H^0 configurations in different parts of the supercell. In all of them the excess electron showed similar trapping characteristics. Similar evidence of electron trapping was observed in our recent first-principles calculations of hydrogen configurations in cubic yttria-stabilized zirconia [31,53]. Similarly, hydrogen was found to be an amphoteric defect exhibiting a deep-donor behavior in its lowest-energy structure.

In order to make connection with the μSR data and analysis and also to quantify these findings through a measurable quantity we calculated the hyperfine tensor, **A**, for these oxygen-bound H^0 states. **A** describes the interaction of the electron spin with the nonzero magnetic moments of the nuclei and can be generally represented by two parts: an isotropic term, $A_{\rm iso}$, and the remaining anisotropic part, $\mathbf{A}_{\rm ani}$, as follows [54]:

$$\mathbf{A} = A_{\rm iso}\mathbf{I} + \mathbf{A}_{\rm ani}, \tag{4}$$

where **I** is the 3×3 identity matrix.

The isotropic part, also known as the Fermi-contact interaction [54], $A_{\rm iso}$, is a measure of the localization character of the hydrogen electron. The specific value of $A_{\rm iso}$ depends upon the magnitude of the electron spin density ρ_s ($\rho_s = \rho_\uparrow - \rho_\downarrow$) at the site **R** of the nucleus as [54]

$$A_{\rm iso} = \frac{8\pi}{3} g_e \mu_e g_H \mu_H \rho_s(\mathbf{R}), \tag{5}$$

where g_e is the electronic g factor, μ_e is the Bohr magneton, $g_{\rm H}$ is the nuclear gyromagnetic ratio for hydrogen, and $\mu_{\rm H}$ is the nuclear magneton. The anisotropic part $\mathbf{A}_{\rm ani}$ accounts for the magnetic dipole-dipole interactions between the electron and the nuclei [49,54].

Diagonalization of the hyperfine tensor can then provide the principal values of the hyperfine interaction, commonly labeled as A_{xx}, A_{yy}, and A_{zz}. From these values the Fermi-contact term $A_{\rm iso}$ is then obtained as $\frac{1}{3}(A_{xx} + A_{yy} + A_{zz})$, and the dipolar ($D$) hyperfine parameter as $D = 2b = 2(A_\parallel - A_\perp)/3$, with $A_\parallel$ being the largest of the principal values of the hyperfine tensor and $A_\perp$ the average of the remaining two.

The $A_{\rm iso}$ and D values were determined for four different oxygen-bound H^0 configurations using the PBE functional and for one (the one possessing the lowest-formation energy) using the hybrid HSE06 functional.

The obtained $A_{\rm iso}$ values were extremely small, in all cases less than 1 MHz and even equal to zero for one of the studied configurations. These findings are indicative of a vanishing (almost nonexistent) spin density at the site of the hydrogen nucleus. The lowest-energy neutral bond configuration (depicted in Fig. 4), in particular, was found to possess a Fermi-contact term with a magnitude of 0.64 MHz using the PBE functional and 0.45 MHz using the HSE06 functional. The same oxygen-bound configuration also possessed a dipolar hyperfine constant D equal to 2.4 MHz (a result by means of the HSE06 hybrid functional). The corresponding result by the PBE functional was also very similar (2.2 MHz). PBE calculations of the dipolar part D for the other higher-energy configurations showed some variation: although one configuration possessed exactly the same magnitude of D as the lowest-energy structure, two others had markedly smaller dipolar parts (equal to 0.9 MHz). These variations in the value of D suggest a dependence of the anisotropic hyperfine interaction upon the angular distribution of the spin density with respect to the hydrogen site as well as upon the distance between the hydrogen nucleus and the Zr ion which carries most of the spin density.

These calculations clearly show that the oxygen-bound configuration is characterized by a small value of the hyperfine interaction, dominated by the dipolar component.

B. μSR

As will be discussed in detail below, we assign the diamagnetic and paramagnetic p_1 components described in Sec. II A to the oxygen-bound configuration presented in Sec. III A. However the diamagnetic site has a Zr^{4+} ion neighbor and the paramagnetic p_1 site has a Zr^{3+} polaron neighbor. This paramagnetic component is thus characterized by a very small hyperfine interaction dominated by the dipolar component, as discussed in Sec. III A, so that its direct spectroscopic separation from the diamagnetic component is not possible and is achieved through the investigation of the line broadening.

The temperature dependence of the paramagnetic relaxation λ_{p_1} is presented in Fig. 5. At the lowest temperatures, this relaxation is about one order of magnitude higher than the diamagnetic relaxation σ and thus easily distinguishable. However, λ_{p_1} decreases as temperature increases up to room

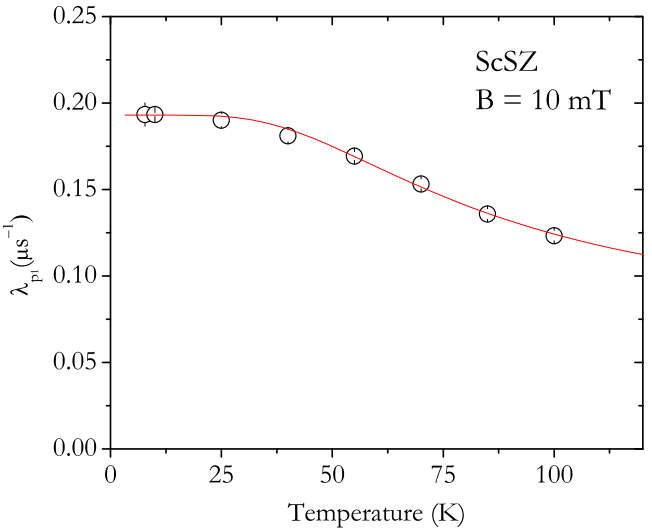

FIG. 5. Temperature dependence of the slowly relaxing paramagnetic relaxation λ_{p1} for the ScSZ sample. The line is a fit as detailed in the text.

TABLE II. Fitted fractions and relaxations for the different samples at the indicated temperatures. The applied transverse field is 10 mT. The diamagnetic relaxation was fixed to $\sigma = 0.03\ \mu s^{-1}$ to all samples. The indicated errors represent the statistical errors obtained directly from fitting. As discussed in the text, the systematical errors are higher.

Sample	T (K)	f_d (%)	f_{p_1} (%)	f_{p_2} (%)	$f_{\rm miss}$ (%)	λ_{p_1} (μs^{-1})	λ_{p_2} (μs^{-1})
ZrO_2 (undoped)	7.8	16(1)	21(1)		63(2)	0.20(2)	
ScSZ	7.8	16(1)	79(2)		5(2)	0.19(1)	
YSZ	8.6	15.2(3)	67.3(2)		17.5(4)	0.270(2)	
MgSZ	9.4	16(2)	69(1)	8(2)	7(3)	0.21(1)	1.3(5)
ZrO_2:Ca (monoclinic)	9	18(2)	51(1)	7(2)	24(3)	0.18(1)	1.0(5)
CaSZ (cubic)	10	27(2)	56(2)	7[a]	10(3)	0.20(1)	1.0[a]

[a]Value fixed equal to that of ZrO_2:Ca (monoclinic).

temperature, making the separation increasingly difficult as the two relaxations become similar. Above about 100 K it is no longer possible to separate the two relaxing components in the fits and a single relaxing component was used in the analysis. As shown in Fig. 5, the relaxation gradually approaches a value which is consistent with the Van Vleck relaxation due to dipolar nuclear broadening. In the temperature range 7–100 K, the diamagnetic relaxation is expected to be fairly constant, any effects due to possible motional narrowing being negligible. Preliminary analysis revealed that the asymmetries A_d and A_{p_1} are constant within the above-mentioned temperature range; this is also consistent with the model presented below. For temperatures below 100 K and for each sample, we have thus fixed the asymmetries A_d and A_{p_1} at the lowest temperature value, as well as the diamagnetic relaxation at $\sigma = 0.03\ \mu s^{-1}$.

In Table II we summarize the results of this analysis: we indicate the fractions f_d, f_{p_1}, and f_{p_2} of muons thermalizing in each configuration, as well as the fraction of muon spin polarization which is not observed (missing fraction) $f_{\rm miss}$. The missing fraction likely corresponds to muons thermalizing at the interstitial configurations, and its recovery and dynamics can be analyzed by means of the repolarization curve and of the behavior of the additional relaxing component.

1. Oxygen bound state

We will now discuss the assignment of the diamagnetic fraction f_d and of the slowly relaxing paramagnetic fraction f_{p_1} to muons thermalizing at the oxygen-bound configuration. As mentioned already, the diamagnetic fraction has a very small Gaussian relaxation consistent with that expected from dipolar nuclear broadening (Van Vleck relaxation). This fraction most likely corresponds to muons thermalizing as Mu^+ at the oxygen-bound configuration, according to the theoretical predictions. As usual in μSR experiments, it is not possible to distinguish directly Mu^+ from the negatively charged diamagnetic configuration Mu^-, but the fact that Mu^- requires the capture of two electrons during the thermalization process of the muon makes it always a far less probable process.

As for the slowly-relaxing paramagnetic component f_{p_1} it corresponds to muons in the presence of a nonzero hyperfine interaction. The Lorentzian shape of the relaxation signals the likely dynamical character of this hyperfine interaction, as discussed below. However, the fact that this hyperfine interaction is too small prevents the clear observation of its distinctive powder-pattern spectrum [55], which is here collapsed over the diamagnetic line and manifests itself as an additional broadening [56,57]. An upper bound for the hyperfine interaction can nevertheless be estimated.

In Fig. 6 we present a Fourier transform of a high-statistics spectrum obtained for YSZ at 8.5 K. This Fourier spectrum was obtained using the Lomb method [58]. From the similar case of TiO_2 we know that the hyperfine interaction is mainly dipolar [24,25]. We may immediately estimate its approximate value from the full width at half maximum of the line, yielding $D \approx \lambda/\pi = 0.09$ MHz. The estimated values for D in the samples studied in this work range from the highest value found for YSZ, $D \approx 0.09$ MHz, to the lowest value $D \approx 0.06$ MHz for ZrO_2:Ca (monoclinic), the span likely arising from the small differences in the lattice relaxation around the muon oxygen-bound configuration and the corresponding different distances of the Zr cations.

The nature of this hyperfine interaction can be understood from the theoretically predicted configuration for the neutral-oxygen-bound state, as shown in Fig. 4. There it is predicted that the electron associated with the neutral-oxygen-bound configuration is in fact not centered at the muon, but instead forms a polaronic state with the electron density localized asymmetrically at nearby Zr^{4+} ions, with an extremely small hyperfine interaction dominated by the dipolar component. A careful inspection of Fig. 4 and the corresponding calculations reveals that the electron is spread over three Zr^{4+} ions, although with a dominant weight to one of them. The latter could then be considered to be reduced to Zr^{3+} to a good

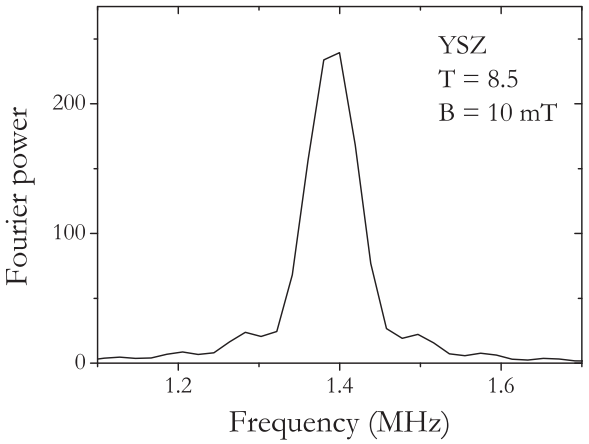

FIG. 6. μSR Fourier spectrum of YSZ at $T = 8.5$ K in an external magnetic field of $B = 10$ mT.

approximation. Such a geometrical arrangement can lead to a large compensation of the dipolar part from different regions of the electron distribution. A similar polaronic state has been proposed for cubic-stabilized zirconia both in electron paramagnetic resonance (EPR) measurements [59,60] and in *ab initio* calculations [31]. These polaronic centers can also be created when samples are irradiated with UV light or x rays or subjected to treatment in hydrogen atmosphere [61]. A polaronic state has also been observed in similar systems, notably TiO_2 [24,25,62]. The difference between the experimental value of the hyperfine interaction and the predicted computational value for the lowest-energy neutral oxygen-bound configuration is probably an indication of spin dynamics [25] or that the lattice does not reach its full relaxed configuration around the muon during the time of the experiment (about 15 μs; see Fig. 2). Furthermore, the fact that the *ab initio* calculations do reveal several minimum-energy oxygen-bound hydrogen configurations (possessing a variety of magnitudes of the dipolar hyperfine constants D) suggests that there may exist additional ones with an even smaller dipolar part, closer to our experimental μSR value. The observed differences in λ_{p_1} for the different samples (Table II) are likely due either to small differences in the distances between the hydrogen/muon neutral-oxygen-bound position and the nearby zirconium atoms or to changes in the electron density distribution.

We now address the temperature dependence of the slow paramagnetic component λ_{p_1}, shown in Fig. 5. We have extracted the activation energy of this mechanism by fitting the data in Fig. 5 with a Boltzmann-like function:

$$\lambda_{p_1}(T) = \frac{1}{1 + N \exp(-E_a/k_B T)}, \tag{6}$$

where E_a is the activation energy of the process, k_B is the Boltzmann constant, and the empirical parameter N relates to the shape of the binding potential. We fixed (after an initial fit with free parameters) the weight factor to $N = 18(3)$ for the monoclinic samples (undoped ZrO_2 and ZrO_2:Ca) and $N = 4(1)$ for the cubic/tetragonal samples (ScSZ and YSZ); an intermediate value of $N = 9(2)$ is found for the mixed MgSZ sample. The results for the activation energies obtained using this analysis are summarized in Table III for all samples except cubic CaSZ, for which we do not have enough experimental data.

The observed decrease of λ_{p1} with temperature is hardly attributed to ionization of the Zr^{3+} polaron, taking into account that EPR data reveal that the corresponding activation energy is at least 0.1 eV for reduced samples [63]. These EPR data do not exclude the existence of spin fluctuations at lower temperatures, which we have discussed in Ref. [64] as an alternative model. Another possibility, in analogy to the H/Mu behavior in TiO_2 [25], is the onset of muon motion between nearly equivalent hydrogen/muon sites. However, the lattice geometry is possibly less favorable in ZrO_2. In fact, Dawson *et al.* [65] calculated activation energies much higher (about 0.4 meV) then those indicated in Table III. As a final alternative, we consider this effect in relation to the formation process of this configuration: the mean distance between the polaron and the muon is bound to increase with temperature, meaning that the electron that comes with the muon and creates the polaron can "thermalize" at longer distances from the muon position. In this likely model, the extracted activation energies in Table III are related to the binding energy of the muon to the electron. We note however that the activation energy is not the full binding energy since there is also a lattice contribution (self-trapping) which may be large. The observed differences in the fractions shown in Table II are probably due to changes in the formation probabilities due to the different crystal structures and to the different cation dopants which likely change the crystal lattice vibrations and therefore affect the final thermalization stages [66]. The same factors affect as well the binding energies shown in Table III.

TABLE III. Activation energies associated with the decrease of the paramagnetic relaxation λ_{p_1} with temperature.

Sample	Binding energy (meV)
ZrO_2 (undoped)	15(1)
ScSZ	15(1)
YSZ	12(1)
MgSZ	5(1)
ZrO_2:Ca (monoclinic)	7(1)

2. *Atom-like interstitial state*

A notable feature shown in Table II is the fact that a significant part of the muon spin polarization is not observed at low temperatures (missing fraction, f_{miss}). As noted above, the fractions (and also the missing fraction) do not vary visibly up to 150 K. The missing fraction is related to muons depolarizing rapidly during the thermalization stage, due to the formation of deeply bound muonium. We thus assign the missing fraction to muons thermalizing in the interstitial configurations discussed in the theory section (either the pure interstitial or the oxygen-vacancy site). The hyperfine interaction associated with these configurations can be nevertheless characterized by means of the longitudinal-field repolarization technique, where the hyperfine interaction is progressively quenched by the increase of an applied longitudinal field. This technique makes use of the fact that for high fields the Zeeman interaction dominates and the depolarizing effect of the hyperfine interaction is quenched.

We note that the repolarization curve of undoped monoclinic zirconia has already been published in Ref. [19] and is consistent with a vacuum-like state. We have now performed repolarization studies for ZrO_2:Ca (monoclinic) and YSZ (Figs. 7 and 8, respectively; Fig. 8 was first presented in a preliminary version of this work [64]), which show remarkable differences. The repolarization curve for ZrO_2:Ca shown in Fig. 7 presents the monotonic increase characteristic of a deep isotropic state. The curve in Fig. 7 is a fit with the usual isotropic repolarization curve [56,67], yielding a hyperfine parameter $A_{\mathrm{iso}} = 3.02(8)$ GHz, characteristic of a deep compact state. However, the repolarization curve for YSZ presented in Fig. 8 is two-stepped, which is a usual sign of anisotropy [68]. We have thus fitted the data in Fig. 8 with the phenomenological repolarization functions proposed by Pratt in Ref. [68] and obtained $A_{\mathrm{iso}} = 2.1(2)$ GHz and $D = 0.13(2)$ GHz.

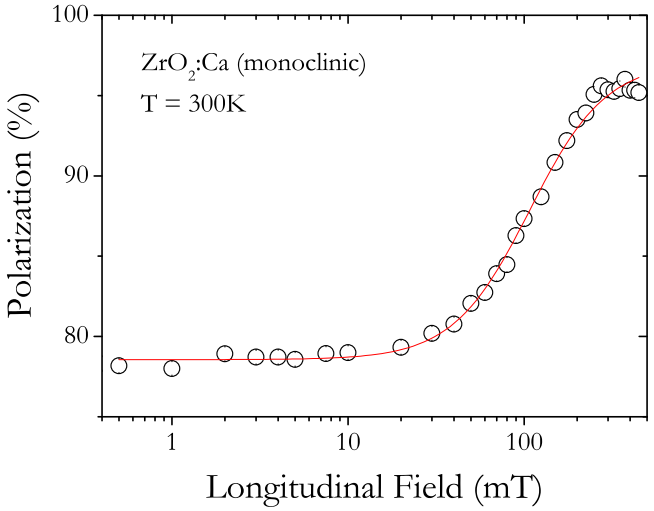

FIG. 7. Repolarization curve for ZrO_2:Ca (monoclinic) at $T = 300$ K. The red line is a fit assuming an isotropic hyperfine interaction $A = 3.02(8)$ GHz.

The corresponding fit is shown as a red line in Fig. 8. Alternatively, the repolarization curve in Fig. 8 can be fitted to a combination of two isotropic states with $A_{iso1} = 1.9(1)$ GHz, $A_{iso2} = 0.11(1)$ GHz.

The two-stepped recovery (Fig. 8) could in principle be due to hyperfine interactions of muons at different sites. However, the smaller of the two interactions [$A_{iso2} = 0.11(1)$ GHz] corresponds neither to a value expected for the interstitial site (interstitial muonium hyperfine interactions are on the order of 3 GHz [53]) nor to a value expected for the bound configuration. Therefore, the more likely interpretation is that the two-stepped rise in Fig. 8 is due to an anisotropic interaction [$A_{iso} = 2.1(2)$ GHz and $D = 0.13(2)$ GHz]. The anisotropy may be induced by a slight off-centered position of the interstitial muon in these highly stressed nanograin samples (muon position at or near the surface) [69–71].

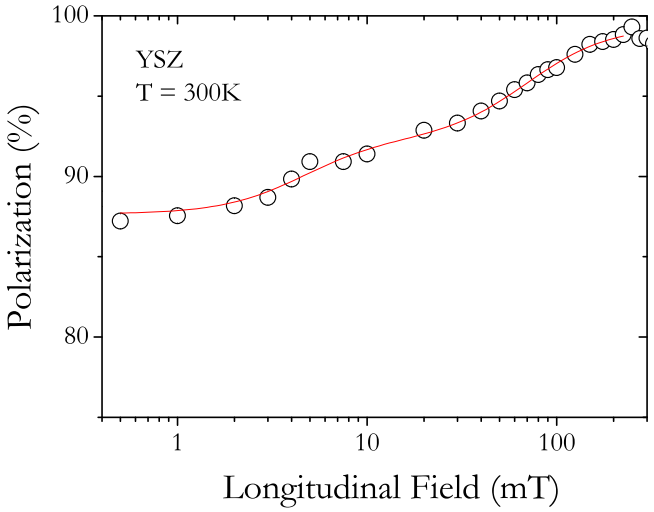

FIG. 8. Repolarization curve for YSZ at $T = 300$ K. The red line is a fit assuming an axially symmetric anisotropic hyperfine interaction with $A_{iso} = 2.1(1)$ GHz and $D = 0.13(2)$ GHz.

A final note with respect to the second relaxing paramagnetic component observed in MgSZ, CaSZ, and ZrO_2:Ca (monoclinic). As shown in Table II, we observed this relaxation in these samples only, with values of the order of 1 μs^{-1}. We note that in monoclinic undoped ZrO_2 an extremely fast relaxation ($\approx 100\ \mu s^{-1}$) was observed in high-field experiments performed at TRIUMF [66]. The f_{p_2} fraction disappears with temperature and is essentially gone at $T \approx 50$ K, although it is not clear whether this is by line broadening or by a reduction of the small fraction of muons f_{p_2} ending up in this state. Similarly to what has been discussed in Ref. [66], delayed muonium formation from a diamagnetic state arises as the most likely assignment. In this model muons stop at the interstitial site as a diamagnetic-like state and slowly convert to Mu^0 at this configuration. The conversion process is delayed because the lattice takes some time to relax to the minimum energy configuration associated with the presence of the impurity.

We note that although atom-like muonium is not observed directly in the transverse field experiments because of dephasing, the fraction of delayed-formed atom-like muonium can nevertheless be obtained from the fraction of the fast-relaxing signal. The longitudinal-field decoupling experiment yields the magnitude of the hyperfine interaction and also an estimate of the formation probability. These results are consistent with the transverse field data.

3. *Interstitial to oxygen bound state transition*

In these transverse-field experiments, we have also addressed the temperature dependence of the YSZ, ScSZ, and monoclinic ZrO_2:Ca samples, as well as that of the undoped monoclinic ZrO_2 sample. Above 200 K muon diffusion seems to play a non-negligible role and we intend to follow up this subject in subsequent work. However, a temperature effect highly relevant to the current discussion of the muonium/hydrogen configurations is apparent at these higher temperatures. As shown in Fig. 9, the total observed fraction of muons gradually grows up to 100% at about 700 K, meaning that the missing fraction f_{miss} is gradually recovered. We recall that at above 200 K the data are adequately described by a single diamagnetic component as discussed in Sec. II A. The temperature dependence of the recovery of the missing fraction is adequately described by a Boltzmann model (Eq. (7)) for all samples:

$$f_d(T) = \frac{f_{d0} N \exp(-E_a/k_B T)}{1 + N \exp(-E_a/k_B T)}. \quad (7)$$

The corresponding activation energies E_a are summarized in Table IV.

TABLE IV. Activation energies of the recovery of the missing fraction (Fig. 9) and associated with the barrier between the atom-like interstitial configuration and the oxygen-bound configuration.

Sample	Activation energy (eV)
ZrO_2 (undoped)	0.26(2)
ScSZ	0.14(3)
YSZ	0.12(2)
ZrO_2:Ca (monoclinic)	0.21(2)

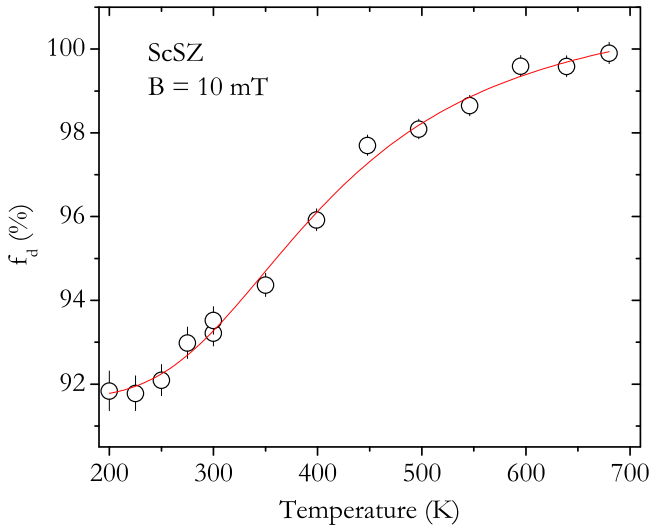

FIG. 9. Observed fraction of muon spin polarization as a function of temperature, in transverse geometry ($B = 10$ mT), for the ScSZ sample. The line is a fit to a Boltzmann model with an activation energy $E_a = 0.14(3)$ eV, which we associate with the barrier between the atom-like interstitial configuration and the oxygen-bound configuration.

The recovery of the missing fraction can arise due to different processes affecting the muons stopping in the neutral muonium state at the interstitial configuration. However, both the loss of the muonium electron to the conduction band ($Mu^0 \rightarrow Mu^+ + e^-_{CB}$) or the capture of an electron from the valence band ($Mu^0 + e^-_{VB} \rightarrow Mu^-$) seem unlikely: the corresponding calculated energies (about 5 eV and 1.35 eV, respectively) are much higher than those measured (Table IV). The capture of the electron released by the polaron in its ionization ($Mu^0 + e^-_{polaron} \rightarrow Mu^-$) also seems unlikely, since Mu^- is likely to be thermally unstable at these high temperatures, which is not consistent with the near absence of relaxation of the observed diamagnetic component. The most likely interpretation for the recovery of the missing fraction shown in Fig. 9 is hence that an alteration of the formation probabilities of the interstitial configuration and of the oxygen bound configuration occurs, in favor of the latter. This interpretation is supported by our recent DFT calculations, where a very small energy barrier (0.1 eV) was determined for hydrogen to transform from the interstitial to its lower-energy oxygen-bound configuration (see Fig. 9 in Ref. [31]). This calculated value is consistent with the experimental values reported in Table IV, which in this interpretation do not relate to the position of the level in the gap, but to the energy barrier between configurations. Interestingly, the experimental values for the monoclinic samples (undoped ZrO_2 and ZrO_2:Ca) are about twice the values of the cubic samples, probably reflecting the fact that the vibration modes with higher oscillator strengths occur at higher energies for the monoclinic lattice than for the cubic lattice [34]. A vibrational level 0.1 eV above the fundamental was already suggested for the interpretation of EPR data in cubic YSZ [63]. The role of vibrations in the formation process of muonium was also suggested for the interpretation of μSR data in HfO_2 [66].

IV. CONCLUSIONS

In summary, from the combination of the above presented *ab initio* calculations and μSR experiments, a rather complete view of the muonium configurations in zirconia is revealed. The same electronic configurations are therefore expected for the isolated hydrogen impurity in zirconia. The local nature of the muon probe allows us to build a unified view despite the doping, crystallographic, and grain-size differences between the samples. In the case of the neutral donor-like configuration at an oxygen-bound position the electron is trapped near the hydrogen nucleus with the corresponding electron density localized at neighboring Zr cations. This particular geometrical arrangement is characterized by a very small hyperfine interaction, dominated by the dipolar component, but the experimental value of the hyperfine interaction is probably further reduced due to fluctuations related to the formation process. The binding energy of the muon to the electron is not larger than 20 meV in this configuration. Neutral atom-like configurations are also observed and characterized by compact wave functions with vacuum-like hyperfine interactions (2–3 GHz), which are isotropic for the monoclinic ZrO_2:Ca sample and slightly distorted for the cubic YSZ sample. The difference between these two interstitial configurations is also visible in the interstitial to oxygen bound barrier that we have characterized. The differences likely arise from the different grain sizes of the samples, where strongly distorted local surroundings are present. The corresponding activation energies for the proton may be slightly different due to the different zero motion of the proton and of the muon. We would nevertheless like to stress the powerful information conveyed by this work with respect to the configuration of the isolated hydrogen impurity in zirconia, not only due to the strict analogy of the experimental electronic configurations of muonium and hydrogen, where no isotopic effects are expected, but also due to the strong complementarity of the experimental and theoretical information here presented.

ACKNOWLEDGMENTS

The technical help of the μSR team at ISIS is gratefully acknowledged. We also thank INNOVNANO for providing the YSZ sample used in this work and acknowledge helpful discussions with João Calado, Elsa Antunes, and Sofia Soares. The computer resources of the Department of Physics of the University of Coimbra were used, including the Milipeia cluster at the Laboratory for Advanced Computing. This work was supported with funds from (i) FEDER (Programa Operacional Factores de Competitividade COMPETE) and from FCT - Fundação para a Ciência e Tecnologia under Projects No. PEst-OE/FIS/UI0036/2014 and No. PTDC/FIS/102722/2008; (ii) European Commission under the 7th Framework Programme through the "Research Infrastructures" action of the "Capacities" Programme, NMI3-II Grant No. 283883, Contract No. 283883-NMI3-II; (iii) Ph.D. Grant No. SFRH/BD/87343/2012 from FCT - Fundação para a Ciência e Tecnologia (R.B.L.V.); (iv) Welch Foundation Grant No. D-1321 (TTU group); (v) QREN-Mais Centro Project No. ICT_2009_02_012_1890 (access to TAIL-UC facility).

[1] G. Eranna, B. C. Joshi, D. P. Runthala, and R. P. Gupta, Crit. Rev. Solid State Mater. Sci. **29**, 111 (2004).

[2] L. B. Chen, Surf. Rev. Lett. **13**, 535 (2006).

[3] V. Firouzdor, J. Brechtl, L. Wilson, B. Semerau, K. Sridharan, and T. R. Allen, J. Nucl. Mater. **438**, 268 (2013).

[4] J. Robertson, Rep. Prog. Phys. **69**, 327 (2006).

[5] N. Mahato, A. Banerjee, A. Gupta, S. Omar, and K. Balani, Prog. Mater. Sci. **72**, 141 (2015).

[6] S. Kim, H. J. Avila-Paredes, S. Wang, C.-T. Chen, R. A. De Souza, M. Martin, and Z. A. Munir, Phys. Chem. Chem. Phys. **11**, 3035 (2009).

[7] C. Tandé, D. Pérez-Coll, and G. C. Mather, J. Mater. Chem. **22**, 11208 (2012).

[8] J. M. Gil, H. V. Alberto, R. C. Vilão, J. Piroto Duarte, P. J. Mendes, L. P. Ferreira, N. Ayres de Campos, A. Weidinger, J. Krauser, C. Niedermayer *et al.*, Phys. Rev. Lett. **83**, 5294 (1999).

[9] J. M. Gil, H. V. Alberto, R. C. Vilão, J. Piroto Duarte, N. Ayres de Campos, A. Weidinger, J. Krauser, E. A. Davis, S. P. Cottrell, and S. F. J. Cox, Phys. Rev. B **64**, 075205 (2001).

[10] C. G. Van de Walle, Phys. Rev. Lett. **85**, 1012 (2000).

[11] S. F. J. Cox, E. A. Davis, S. P. Cottrell, P. J. C. King, J. S. Lord, J. M. Gil, H. V. Alberto, R. C. Vilão, J. Piroto Duarte, N. Ayres de Campos *et al.*, Phys. Rev. Lett. **86**, 2601 (2001).

[12] R. C. Vilão, A. G. Marinopoulos, R. B. L. Vieira, A. Weidinger, H. V. Alberto, J. Piroto Duarte, J. M. Gil, J. S. Lord, and S. F. J. Cox, Phys. Rev. B **84**, 045201 (2011).

[13] E. L. Silva, A. G. Marinopoulos, R. C. Vilão, R. B. L. Vieira, H. V. Alberto, J. Piroto Duarte, and J. M. Gil, Phys. Rev. B **85**, 165211 (2012).

[14] E. L. da Silva, A. G. Marinopoulos, R. B. L. Vieira, R. C. Vilão, H. V. Alberto, J. M. Gil, R. L. Lichti, P. W. Mengyan, and B. B. Baker, Phys. Rev. B **94**, 014104 (2016).

[15] R. L. Lichti, K. H. Chow, J. M. Gil, D. L. Stripe, R. C. Vilão, and S. F. J. Cox, Physica B (Amsterdam) **376–377**, 587 (2006).

[16] R. C. Vilão, J. M. Gil, A. Weidinger, H. V. Alberto, J. Piroto Duarte, N. Ayres de Campos, R. L. Lichti, K. H. Chow, and S. F. J. Cox, Nucl. Instrum. Methods Phys. Res., Sect. A **580**, 438 (2007).

[17] R. L. Lichti, K. H. Chow, and S. F. J. Cox, Phys. Rev. Lett. **101**, 136403 (2008).

[18] S. F. J. Cox, R. L. Lichti, J. S. Lord, E. A. Davis, R. C. Vilão, J. M. Gil, T. D. Veal, and Y. G. Celebi, Phys. Scr. **88**, 068503 (2013).

[19] S. F. J. Cox, J. L. Gavartin, J. S. Lord, S. P. Cottrell, J. M. Gil, H. V. Alberto, J. Piroto Duarte, R. C. Vilão, N. Ayres de Campos, D. J. Keeble *et al.*, J. Phys.: Condens. Matter **18**, 1079 (2006).

[20] P. D. C. King, R. L. Lichti, Y. G. Celebi, J. M. Gil, R. C. Vilão, H. V. Alberto, J. Piroto Duarte, D. J. Payne, R. G. Egdell, I. McKenzie *et al.*, Phys. Rev. B **80**, 081201 (2009).

[21] J. M. Gil, H. V. Alberto, R. C. Vilão, J. Piroto Duarte, N. A. de Campos, A. Weidinger, E. A. Davis, and S. F. J. Cox, J. Phys.: Condens. Matter **13**, L613 (2001).

[22] J. S. Lord, S. F. J. Cox, H. V. Alberto, J. Piroto Duarte, and R. C. Vilão, J. Phys.: Condens. Matter **16**, S4707 (2004).

[23] V. Kolkovsky, V. Kolkovsky, K. Bonde Nielsen, L. Dobaczewski, G. Karczewski, and A. Nylandsed Larsen, Phys. Rev. B **80**, 165205 (2009).

[24] A. T. Brant, S. Yang, N. C. Giles, and L. E. Halliburton, J. Appl. Phys. **110**, 053714 (2011).

[25] R. C. Vilão, R. B. L. Vieira, H. V. Alberto, J. M. Gil, A. Weidinger, R. L. Lichti, B. B. Baker, P. W. Mengyan, and J. S. Lord, Phys. Rev. B **92**, 081202 (2015).

[26] Y. A. Mantz and R. S. Gemmen, J. Phys. Chem. C **114**, 8014 (2010).

[27] J. L. Lyons, A. Janotti, and C. G. Van de Walle, Microelectron. Eng. **88**, 1452 (2011).

[28] P. W. Peacock and J. Robertson, Appl. Phys. Lett. **83**, 2025 (2003).

[29] K. Xiong, J. Robertson, and S. J. Clark, J. Appl. Phys. **102**, 083710 (2007).

[30] M. Youssef and B. Yildiz, Phys. Chem. Chem. Phys. **16**, 1354 (2014).

[31] A. G. Marinopoulos, Phys. Rev. B **86**, 155144 (2012).

[32] H. Li and J. Robertson, J. Appl. Phys. **115**, 203708 (2014).

[33] A. X. S. Bruker, TOPAS V4: General Profile and Structure Analysis Software for Powder Diffraction Data, Users Manual, Karlsruhe, Germany, 2008.

[34] X. Zhao and D. Vanderbilt, Phys. Rev. B **65**, 075105 (2002).

[35] J. S. Park, Y. B. Kim, J. H. Shim, S. Kang, T. M. Gür, and F. B. Prinz, Chem. Mater. **22**, 5366 (2010).

[36] F. L. Pratt, Physica B (Amsterdam) **289–290**, 710 (2000).

[37] P. Hohenberg, Phys. Rev. **136**, B864 (1964).

[38] W. Kohn and L. J. Sham, Phys. Rev. **140**, A1133 (1965).

[39] J. P. Perdew, K. Burke, and M. Ernzerhof, Phys. Rev. Lett. **77**, 3865 (1996).

[40] J. Paier, M. Marsman, K. Hummer, G. Kresse, I. C. Gerber, and J. G. Angyán, J. Chem. Phys. **124**, 154709 (2006).

[41] J. Paier, M. Marsman, K. Hummer, G. Kresse, I. C. Gerber, and J. G. Angyán, J. Chem. Phys. **125**, 249901 (2006).

[42] M. Marsman, J. Paier, A. Stroppa, and G. Kresse, J. Phys.: Condens. Matter **20**, 064201 (2008).

[43] P. E. Blöchl, Phys. Rev. B **50**, 17953 (1994).

[44] G. Kresse and D. Joubert, Phys. Rev. B **59**, 1758 (1999).

[45] G. Kresse and J. Hafner, Phys. Rev. B **47**, 558 (1993).

[46] G. Kresse and J. Hafner, Phys. Rev. B **49**, 14251 (1994).

[47] G. Kresse and J. Furthmuller, Phys. Rev. B **54**, 11169 (1996).

[48] P. E. Blöchl, Phys. Rev. B **62**, 6158 (2000).

[49] K. Szász, X. T. Trinh, N. T. Son, E. Janzén, and A. Gali, J. Appl. Phys. **115**, 073705 (2014).

[50] D. W. Strickler and W. G. Carlson, J. Am. Ceram. Soc. **48**, 286 (1965).

[51] M. Zacate, Solid State Ionics **128**, 243 (2000).

[52] F. Pietrucci, M. Bernasconi, A. Laio, and M. Parrinello, Phys. Rev. B **78**, 094301 (2008).

[53] A. G. Marinopoulos, J. Phys.: Condens. Matter **26**, 025502 (2014).

[54] J.-M. Spaeth and H. Overhof, *Point Defects in Semiconductors and Insulators: Determination of Atomic and Electronic Structure from Paramagnetic Hyperfine Interactions* (Springer, Berlin, 2003).

[55] H. V. Alberto, R. C. Vilão, J. Piroto Duarte, J. M. Gil, N. Ayres de Campos, R. L. Lichti, E. A. Davis, S. P. Cottrell, and S. F. J. Cox, Hyperfine Interact. **136/137**, 471 (2001).

[56] B. Patterson, Rev. Mod. Phys. **60**, 69 (1988).

[57] J. Piroto Duarte, Ph.D. thesis, University of Coimbra, 2006, http://hdl.handle.net/10316/2533.

[58] N. R. Lomb, Astrophys. Space Sci. **39**, 447 (1976).
[59] C. B. Azzoni and A. Paleari, Phys. Rev. B **40**, 6518 (1989).
[60] V. M. Orera, R. I. Merino, Y. Chen, R. Cases, and P. J. Alonso, Phys. Rev. B **42**, 9782 (1990).
[61] C. Azzoni, Solid State Ionics **44**, 267 (1991).
[62] F. Bekisli, W. B. Fowler, and M. Stavola, Phys. Rev. B **86**, 155208 (2012).
[63] C. Azzoni and A. Paleari, Solid State Ionics **46**, 259 (1991).
[64] R. B. L. Vieira, R. C. Vilão, P. M. Gordo, A. G. Marinopoulos, H. V. Alberto, J. Piroto Duarte, J. M. Gil, A. Weidinger, and J. S. Lord, J. Phys.: Conf. Ser. **551**, 012050 (2014).
[65] J. A. Dawson, H. Chen, and I. Tanaka, Phys. Chem. Chem. Phys. **16**, 4814 (2014).
[66] R. B. L. Vieira, R. C. Vilão, H. V. Alberto, J. M. Gil, A. Weidinger, B. B. Baker, P. W. Mengyan, and R. L. Lichti, J. Phys.: Conf. Ser. **551**, 012048 (2014).
[67] B. Eisenstein, R. Prepost, and A. M. Sachs, Phys. Rev. **142**, 217 (1966).
[68] F. L. Pratt, Philos. Mag. Lett. **75**, 371 (1997).
[69] A. J. Houtepen, J. M. Gil, J. S. Lord, P. Liljeroth, D. Vanmaekelbergh, H. V. Alberto, R. C. Vilão, J. Piroto Duarte, N. Ayres de Campos, J. L. Gavartin *et al.*, Physica B (Amsterdam) **404**, 837 (2009).
[70] G. M. Dalpian and J. R. Chelikowsky, Phys. Rev. Lett. **96**, 226802 (2006).
[71] T.-L. Chan, M. L. Tiago, E. Kaxiras, and J. R. Chelikowsky, Nano Lett. **8**, 596 (2008).